Journal of Structural Geology 32 (2010) 566–579

Contents lists available at ScienceDirect

Journal of Structural Geology

journal homepage: www.elsevier.com/locate/jsg

A model for low amplitude detachment folding and syntectonic stratigraphy based on the conservation of mass equation

J. Contreras*

Departamento de Geología, Centro de Investigación Científica y de Educación Superior de Ensenada (CICESE), km 107 carretera Tijuana-Ensenada, Ensenada, BC 22860, Mexico

ARTICLE INFO

Article history:
Received 10 June 2009
Received in revised form
8 March 2010
Accepted 11 March 2010
Available online 20 March 2010

Keywords:
Stratigraphic modeling
Detachment folding
Growth strata
Self-affine deformation

ABSTRACT

This paper presents a model for the structural evolution of low strain detachment folds in which rock is treated as an incompressible deformable material and its kinematics is governed by the continuity equation. The model also considers the following boundary conditions: (*i*) the vertical flux across the core of the fold is described by a cosine function, (*ii*) the horizontal flux due to transport along a basal detachment remains constant with depth, and (*iii*) the depth of the detachment remains fixed. Upon finding analytical expressions for the velocity field of this deformation process, a model for the accumulation of growth strata and the degradation of the topography created by folding is then derived. These processes are approximated by means of the transport-diffusion equation.

Solutions of these two models are in excellent agreement with geometric, and stratigraphic relations documented in fold-and-thrust belts, and analog experiments. Moreover, the model indicates that fold growth in this class of structures is a *self-affine* process. A compilation of detachment folds around the world indicates that these structures share a common profile. Moreover, fold amplitude and wavelength of these folds are scaled by different amounts, confirming this result. The stratigraphy obtained with the growth strata model exhibits the typical thinning, and truncation of timelines toward the core of the anticline, cross-cutting relations often observed in seismic cross-sections and field data.

© 2010 Elsevier Ltd. All rights reserved.

1. Introduction

Detachment folds (Fig. 1) are one of the three architectural elements of thrustbelts; the other two being fault-bend folds and fault-propagation folds (Suppe, 1985; Jamison, 1987; Mitra, 1990; Suppe and Medwedeff, 1990; Nemčok et al., 2005). Despite their importance as the building blocks of contractional terrains, little progress has been made toward finding analytical solutions describing the evolution of these structures. Analytical solutions provide with the exact behavior of the system being modeled in terms of well-known elementary functions and material parameters. Moreover, characteristic times and lengths can be readily identified that may reveal fundamental relationships that can be tested against datasets. Of course only the simplest cases have closed-form solutions, and even those are highly idealized.

This work is also motivated by the shortcomings in many of the existing kinematic models of fault-related folding that assume bed length is conserved, and a stylized geometry in which folds are straight-limbed and sharp hinged (Suppe, 1983; Hardy, 1995; Hardy and Poblet, 1995; Contreras and Suter, 1990, 1997; Zehnder and Allmendinger, 2000; Suppe et al., 2004; Hardy and Connors, 2006). A further criticism is that these models consider fault-related folding as a steady state process (Poblet et al., 2004). Some of these assumptions are not physically realistic (e.g., Kwon et al., 2005) and appear to be unwarranted in the light of field data (Wiltschko and Chapple, 1977; Vergés et al., 1996; Poblet et al., 2004), experimental results (Biot, 1961; Storti et al., 1997; Daëron et al., 2007), and other stratigraphic relationships discussed below.

Within this context kinematic models for low amplitude detachment folds and associated growth strata are illustrated here. I selected low amplitude detachment folds because, as it is shown in Fig. 1, they have simple geometries and growth strata. In this figure the pre-growth sequences display a smooth symmetrical shape. Sharp hinges, an idealization often made in the literature (e.g., Poblet and Hardy, 1995; Poblet et al., 1997), are not evident. Instead, fold curvature seems to change evenly from a maximum value at the crest of the structure to a minimum value toward the flanking synclines. Syntectonic strata also display a strong symmetry indicating that these structures grow by acquiring amplitude as shortening is accommodated by folding. All these features suggest that strain is accommodated in a continuous and smooth fashion and that periodic functions are best suited to model the evolution of this class of folds.

* corresponding author
E-mail address: juanc@cicese.mx

0191-8141/$ – see front matter © 2010 Elsevier Ltd. All rights reserved.
doi:10.1016/j.jsg.2010.03.006

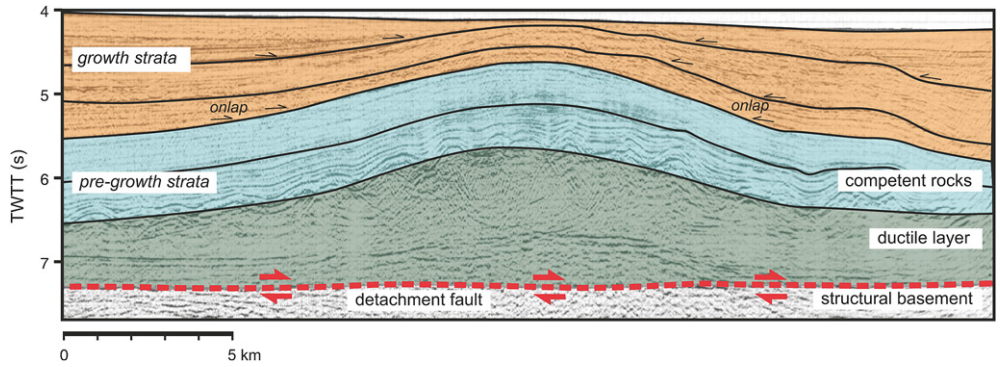

Fig. 1. Example of a detachment fold from the Campos and Santos basin, offshore Brazil (Demercian et al., 1993). These structures form by flow of ductile rocks and by parallel folding of more competent rocks. The stratigraphy of these structures consists of two successions: the pre-growth strata, deposited previous to folding, with a homogenous thickness, and growth strata synchronous with folding.

Existing kinematic models of detachment folding often treat independently axial surface activity, limb rotation, limb lengthening, uplift rate, as well as the accumulation of syntectonic sediments (e.g., Hardy and Poblet, 1994; Poblet and McClay, 1996; Poblet et al., 1997; Wilkerson et al., 2004; Daëron et al., 2007). Even if mass conservation is imposed, additional geometrical constrains such as self-similarity (or the lack of) are required to bring the number of degrees of freedom to a few manageable parameters. Moreover, velocity fields in these works are derived in a heuristic manner, not ab initio. The model presented here is of extreme simplicity. It only considers that mass is conserved, a stationary Eulerian velocity field, and a constant shortening rate applied on the limbs of the structure. These conditions severely restrict the kinematics and time-evolution of folding in the model and reduce the number of free variables to the rate of tectonic uplift, the coefficient of mass diffusion, and the initial dimensions of the fold. In spite of its simplicity, the model reproduces accurately the shape of these folds, their kinematics, and stratigraphic relations observed in seismic lines and analog experiments.

Following the principles of fluid dynamics and previous work by Waltham and Hardy (1995), Hardy and Poblet (1995), and Zehnder and Allmendinger (2000), I start by posing the boundary value problem describing the kinematics of detachment folding and growth strata, as well as their solutions, in an Eulerian reference frame that describes the motion of material points passing through fixed positions in space. Next, the pathlines of the deformation process are obtained; results are then expressed in a more natural Lagrangian reference frame that follows the motion of parcels through time and space. This shift in reference frame is necessary to compare the model results with measurements in analog experiments that track the evolution of material markers through time as deformation progresses. I will refer to positions and velocity components in the Eulerian reference system using capital letters, i.e., X, Y, and V_X, V_Y; for the Lagrangian reference frame I will use lower case letters, i.e., x, y, and v_x, v_y.

Also following the approach of Hardy and Poblet (1994), Hardy et al. (1996) and den Bezemer et al. (1999) the accumulation of growth strata is modeled by means of a boundary value problem in which the topography generated by detachment folding degrades by the combined effects of erosion and sedimentation. These processes are approximated by the transport-diffusion equation whose expression can also be derived from the principle of mass conservation. Once the solution of the boundary value problem is found, the stratigraphic timelines can be obtained by evaluating the solution for past times; bundles of those lines can be compared with sedimentary sequences, which are strata bounded by surfaces that are assumed to represent time lines (e.g., Mial, 1997).

2. The mass conservation equation and other fundamental relations

The mass conservation equation states that the mass change inside an arbitrary volume v fixed in space is equal to the mass flux crossing the bounding surface Γ of the volume, plus the mass added by sources inside the volume. The equation in its integral form is expressed as follows:

$$\int_v \left(\frac{\partial}{\partial t} + \boldsymbol{V}\cdot\nabla\right)\rho \, \mathrm{d}v = \int_\Gamma \boldsymbol{q}\cdot\boldsymbol{n} \, \mathrm{d}\Gamma + \int_v \dot{\varphi} \, \mathrm{d}v, \tag{1}$$

where t is the time, ρ is the mass density, $\boldsymbol{V}$ is the Eulerian velocity, $\boldsymbol{q}$ is the mass flux, $\boldsymbol{n}$ is the unit vector normal to the bounding surface Γ, and $\dot{\varphi}$ represents the mass sources. The differential operator $(\partial/\partial t + \boldsymbol{V}\cdot\nabla)$ is the Lagrangian derivative; the first term is the Eulerian (spatial) derivative whereas the second term represents advection or simply the mass transported by the deforming medium. Specialized forms of this general equation can be derived to characterize the kinematics of deformation as well as the redistribution of mass associated with erosion and sedimentation and are discussed next.

Two assumptions can be made to derive a simpler equation than that of expression (1) governing the kinematics of deformable bodies. The first one is to assume that rocks do not undergo chemical reactions or phase changes. A second assumption is to consider that no expulsion of intra-granular fluids takes place during the burial of sediments. Under such conditions the system remains closed (i.e., there are no sources or sinks of mass), and ρ is constant. Expression (1) then simplifies to the continuity equation (Landau and Lifshitz, 1987):

$$\frac{\partial V_X}{\partial X} + \frac{\partial V_Y}{\partial Y} = 0. \tag{2}$$

Observe that both the identity $\boldsymbol{q} = \rho\boldsymbol{V}$ and the divergence theorem were used to obtain this last result.

Now, the pathlines that material points describe as deformation progresses are the family of curves $\boldsymbol{\sigma}(X, Y, t)$ that satisfy the following differential equation (Landau and Lifshitz, 1987):

$$\frac{\mathrm{d}\boldsymbol{\sigma}}{\mathrm{d}t} = \boldsymbol{V}(\boldsymbol{\sigma}), \tag{3}$$

with initial conditions $\boldsymbol{\sigma}(X, Y, t = 0) = (x, y)$, where (x, y) correspond to positions of material points in the initial configuration. It should be apparent that the deformation function $\boldsymbol{f}$, the mapping

that relates material points in the initial configuration to points in the deformed state, is simply

$$\boldsymbol{f}(x, y) = \boldsymbol{\sigma}(x, y, t). \quad (4)$$

Where rocks are exposed to weathering and transport agents, a redistribution of mass takes place in the form of erosion and sedimentation that produces changes in elevation of the landscape. The equation that describes these phenomena can be derived from Eq. (1) by expressing the differential volume dv as a column of height h with respect to an arbitrary datum and base dA. Eq. (1) can then be expressed in differential form as (Waltham and Hardy, 1995; Hardy and Poblet, 1995)

$$\rho\left(\frac{\partial h}{\partial t} + V_X\frac{\partial h}{\partial X} + V_Y\right) = -\frac{\partial q}{\partial X} + \dot{\varphi}. \quad (5)$$

In this last equation the flux term q now corresponds to a superficial flux of sediments carried in suspension by streams. Observations indicate that in transport-limited hillslopes with angles $< 30°$ the flux of sediments is proportional to the gradient of the topography $q = K(\partial h/\partial x)$, where K is the coefficient of mass transport, a constant that determines the rate of transport and erodibility of rocks (Culling, 1963; Carson and Kirkby, 1972). If this is the case, then the rates of erosion and (local) sedimentation are proportional to the curvature of the topography, i.e.,

$$\frac{\partial h}{\partial t} + V_X\frac{\partial h}{\partial X} + V_Y = -\kappa\frac{\partial^2 h}{\partial X^2} + \dot{s}, \quad (6)$$

where $\kappa = K/\rho$ is the coefficient of mass diffusion, and $\dot{s} = \dot{\varphi}/\rho$ represents sediments derived from far sources that settle on top of the topography at a constant sedimentation rate. Eq. (6) describes the evolution of topography and growth strata in tectonically active areas and is applicable to landscapes with a constant topographic profile along strike where colluvium is readily available for transport (Nash, 2005); this equation properly accounts, albeit in a simplified manner, for the effects of erosion, sedimentation, advection of topography, and deposition of sediments from distant sources at the length scale of detachment folding. This is, at larger length scales erosion, sedimentation, and deformation become highly non-linear coupled processes (e.g., Cloetingh et al., 1999; Garcia-Castellanos et al., 2003).

3. Detachment folding model

The model is restricted to a class of fault-related folds denominated low amplitude detachment folds (Wiltschko and Chapple, 1977; Mitra, 2003; González-Mieres and Suppe, 2006), which are structures with a small amount of contraction. That is, I do not consider folds with a high amplitude/wavelength ratio. For large deformations, detachment folds become disharmonic and not all of the deformation is accommodated continuously, which results in the development of kink bands, faults, and layer-parallel shearing (Fig. 2; Jamison, 1987; Storti et al., 1997; Mitra, 2003).

In the models I consider, the fold axis is taken to be stationary. The core of the structure, therefore, rises vertically with time and the surrounding rock deforms around it. If the fold is moving at a uniform velocity v_f, then model results can be recast for such an inertial moving frame by means of a simple Galilean transformation.

In order to restrict the model further, I will only consider detachment folds with a homogeneous stratigraphy. In the case in which a strong rheological layering is present (e.g., the many classic detachment folds of the Jura Mountains), the model probably accurately describes the behavior of the ductile layers as long as they deform by parallel-to-bed pure shear and not by dislocation flow (Wiltschko and Chapple, 1977).

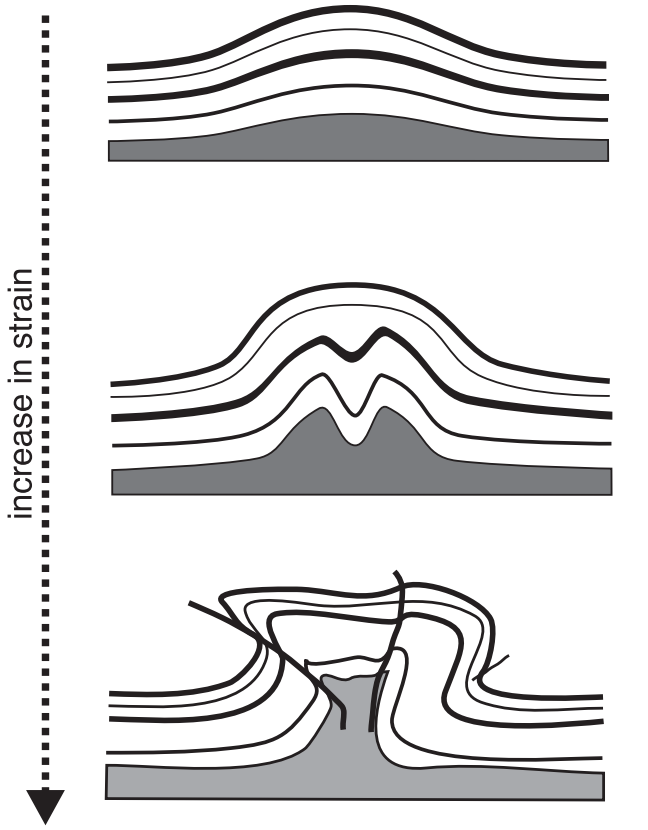

Fig. 2. Progression of deformation in detachment folds based on observations in the Jura Mountains, Switzerland, and the Tian Shan Piedmont, Central Asia. The detachment surface lies at the base of the gray basal layer (based on Jamison, 1987; Storti et al., 1997; Mitra, 2003; Hubert-Ferrari et al., 2007).

The model consists of a rectangular region of thickness H and half-length L that buckles under the action of compressional stresses, becoming decoupled from the rocks of the tectonic basement along a shear zone or detachment surface (Fig. 3A). The following boundary conditions are imposed. (*i*) Tectonic stresses contract the tabular region at a constant shortening rate v_s. The mass flux (ρv_s), therefore, is constant with depth at $X = L$. This is in agreement with the observations made by González-Mieres and Suppe (2006) who have shown that there is no layer-parallel simple shear, i.e., shortening remains constant as a function of depth. (*ii*) The upward mass flux normal to the compression forces at $Y = H$ follows a cosine function. The mass flux is maximum at the core of the detachment fold reaching a constant value of ρv_u, where v_u is the tectonic uplift rate. The wavelength of the fold remains constant with depth, a condition required to satisfy (*i*). Well-imaged detachment folds indicate that some of these structures do deform in that way (Wiltschko and Chapple, 1977; Epard and Groshong, 1993; Epard and Groshong, 1995; Hubert-Ferrari et al., 2007). (*iii*) The horizontal and vertical components of the velocity field vanish along the fold axis and the basal detachment, respectively. The derivation of a solution that satisfies these constraints can be found in Appendix A. The solution is given by the following expressions:

$$V_X = -\frac{v_u L}{2\pi H}\sin(\pi X/L) - \frac{v_u X}{2H}, \quad (7)$$

$$V_Y = \frac{v_u Y}{2H}\cos(\pi X/L) + \frac{v_u Y}{2H}. \quad (8)$$

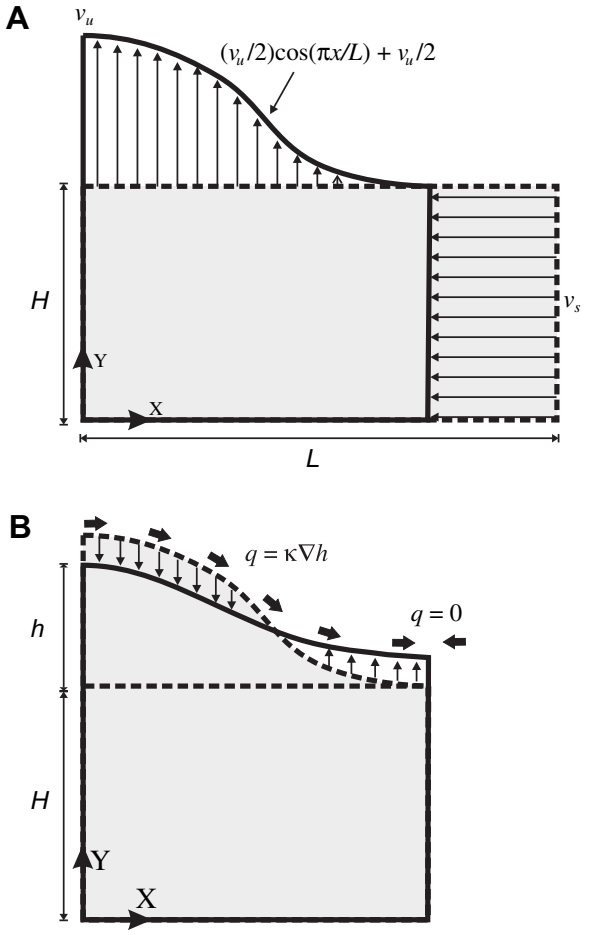

Fig. 3. A) Geometry and boundary conditions of the detachment fold model presented in this paper. It consists of a rectangular region with dimensions $L \times H$. The rate of shortening on v_s on the right side of the region remains constant with depth, whereas the mass flux at the core of the structure follows a cosine function with a maximum rate of uplift v_u. (B) Sketch of the erosion and sedimentation model. Flux of material downslope q is proportional to the topographic gradient. The model assumes periodical boundary conditions; as a result, the flux of mass leaving the boundary at right cancels out with the incoming flux from neighboring folds.

To calculate the pathlines that material points describe, as shortening is accommodated by folding, it is necessary to solve Eq. (3). Appendix A presents an approximate solution to this equation valid near the core of the detachment fold. The solution consists of the following expressions:

$$\sigma_X = \sigma_X^0 \exp(-tv_u/H) \tag{9}$$

$$\sigma_Y = \sigma_Y^0 \exp\left(tv_u\left[\cos\left(\pi\sigma_X^0/L\right)+1\right]/2H\right). \tag{10}$$

In the previous equations, one can identify σ_X^0 and σ_Y^0 with the material positions of particles (x, y) in the undeformed state at $t = 0$, and σ_X and σ_Y with the spatial position (X, Y) of particles in the deformed state. Then the deformation function for detachment folding is

$$X = x \exp(-tv_u/H), \tag{11}$$

$$Y = y \exp(tv_u[\cos(\pi x/L)+1]/2H). \tag{12}$$

These last two equations describe how shortening is accommodated in the model (Eq. (11)) and how fold shape evolves through time (Eq. (12)). From expression (12) we can derive three important geometrical parameters of detachment folds used in the balancing of structural cross-sections: the structural relief R, the excess area A_e, and the shortening u (Fig. 4). The structural relief is simply the amplitude of the fold at $X = 0$

$$R = Y - y = y\left(e^{tv_u/H} - 1\right). \tag{13}$$

Now, the excess area is the integral of the uplifted portion

$$A_e = 2\int_0^L y[\exp(tv_u[\cos(\pi x/L)+1]/2H) - 1]dx, \tag{14}$$

and the derivative of A_e with respect to y is the shortening u or, equivalently, the change in bed length ΔL (Epard and Groshong, 1993; González-Mieres and Suppe, 2006):

$$u = \Delta L = 2\int_0^L \exp(tv_u[\cos(\pi x/L)+1]/2H)dx. \tag{15}$$

The last two integral equations, however, do not have closed-form solutions and must be computed numerically.

Two other fundamental parameters that can be obtained from Eqs. (11) and (12) are the scaling factors λ_x and λ_y that describe how fold shape is rescaled at different times and determine whether fold growth is a self-similar process. These are given by the expressions:

$$\lambda_x = e^{-tv_u/H}, \tag{16}$$

$$\lambda_y = e^{tv_u/H}. \tag{17}$$

Finally, the Lagrangian velocity, $\boldsymbol{v}$, which describes the motion of material particles, can be found by differentiating the components of the deformation function (Eqs. (11) and (12)) with respect to time.

$$v_x = \frac{-v_u}{H}x\exp(-tv_u/H) \tag{18}$$

$$v_y = \frac{yv_u}{2H}[\cos(\pi x/L)+1]\exp\left(\frac{tv_u}{2H}\cos(\pi x/L) + \frac{tv_u}{2H}\right) \tag{19}$$

4. Growth strata model

Growth or syntectonic strata (Suppe et al., 1992) are features of interest because they contain information about the timing of deformation events and the rate at which they took place. These strata also impose stringent constraints on the kinematics of deformation that models such as the one presented in this paper must satisfy (Zoetemeijer et al., 1992; Vergés et al., 1996; Poblet et al., 1997; Suppe et al., 1997; Scharer et al., 2006), and many

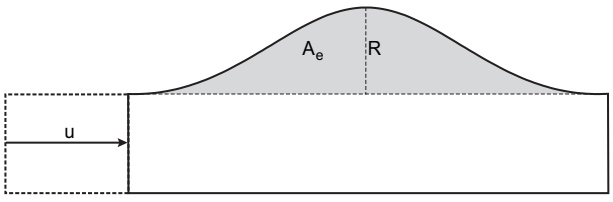

Fig. 4. Geometrical elements of detachment folds. R is the structural relief or amplitude of the fold. A_e is the excess area. This is the area uplifted by folding. u is the linear shortening.

others. For example, syntectonic strata form conformable successions in the flanking synclines, whereas condensed sections and progressive unconformities (Riba, 1976) develop at the fold limbs. Moreover, a strong angular unconformity often develops at the crest of these structures. Another important feature of these strata is that their dip increases with age, i.e., older sediments dip more steeply than do younger sediments.

The idea, then, is to incorporate the effects of erosion and sedimentation into the model of detachment fold to generate a synthetic stratigraphy and see if it can reproduce documented stratigraphic histories in actual folds. This will further validate the detachment model.

The model uses the transport-diffusion Eq. (6) to capture the degradation of the detachment fold by erosion and sedimentation (Fig. 3B). The problem has the following initial and boundary conditions: (*i*) initially, the relief of the model is flat and has an elevation H, and (*ii*) reflective boundary conditions are imposed on the synclinal valley and crest of the anticline. This means that the flux of mass leaving the region across their boundaries cancels out with a similar incoming flux from adjacent detachment folds located farther to the right and left (not shown in Fig. 3). Appendix C presents in detail the derivation of a solution that satisfies these initial and boundary conditions. The expression that describes the evolution of topography is as follows:

$$h = \frac{v_u L^2}{\kappa\pi^2}\left(1 - e^{-t\kappa\pi^2/2L^2}\right)\cos(\pi X/L) + \frac{t v_u}{2} + \dot{s}t + H. \tag{20}$$

Finally, stratigraphic timelines ζ deposited at past times ξ, with respect to the current time t, can be obtained by using the following transformation:

$$\zeta(\xi) = h(X(x,\ t-\xi),\ t-\xi). \tag{21}$$

5. Results

Fig. 5 shows the development of a detachment fold based on Eqs. (11) and (12). The parameters used for this particular solution are those documented by Daëron et al. (2007) for a series folds in the Tian Shan province in Central Asia: $L = 10$ km, $H = 2$ km, and $v_u = 0.25$ mm/yr. Fig. 5A–C illustrates how the initial rectangular region shortens and folds as the constituent material particles travel through the stationary Eulerian velocity field described by Eqs. (7) and (8). The snapshots correspond to $t = 1$, 2, and 3 Ma. Fig. 5D is a plot of the deformed state at 3 Ma in which layers have been included revealing how deformation is accommodated inside the structure. Finally, Fig. 5E is a plot of the pathlines described by the material points. These curves are similar to rectangular hyperbolae with asymptotes given by the coordinate axis.

The degradation of topography as well as the syntectonic depositional patterns associated with the growth of a detachment fold is presented in Fig. 6. Geometrical and kinematical parameters are the same as in Fig. 5. Two sources of sediments were considered for this example: sediments derived locally by diffusion of the topography and sediments derived from distant sources that settle at a constant rate. The mass diffusivity constant has a value $\kappa = 1.5 \times 10^{-5}$ m^2/s, the far-source sediment supply $\dot{s} = 0.2$ mm/yr, and timelines are drawn every 330 kyr.

Initially timelines of growth strata lie conformably and are indistinguishable from the pre-growth strata except for a slight decrease in thickness toward the fold crest (Fig. 6A). The reason is that erosion and local sedimentation are proportional to the curvature of the topography, which is initially flat. As the fold gains curvature by increasing its structural relief, the crest of the structure starts to erode. Consequently, the thickness of growth strata in the model decreases, developing a thinning-upward pattern similar to the one observed in seismic cross-sections (Fig. 6B and C). The model, however, clearly shows spurious growth strata patterns on the limbs of the anticlines flanking the central fold. The deformation function derived here is only accurate near the core of the central structure.

Fig. 7 assesses how changes in the coefficient of mass diffusion and the external sediment supply affect the development of syntectonic grow strata and the evolution of topography. This figure presents four different cases in which the mass diffusion coefficient κ is set to 10^{-4} and 10^{-6} m^2/yr, and the far-source sediment supply $\dot{s}$ is set to 0.5 and 0.1 mm/yr; all other parameters are those of Fig. 5. It can be seen that the coefficient of mass diffusion controls the amplitude of the eroded topography. A high mass diffusion coefficient results in flat topography, whereas low diffusivity results in an emerging detachment fold. By contrast, sediment supply dictates the development of stratigraphic patterns in the model, an effect also noticed by Hardy and Poblet (1995). The solution with a high sediment supply results, initially, in a covered anticline in which timelines thin upward. Eventually the thinning-upward is replaced by the development of an onlap pattern on the limbs of the structure. Solutions with a low sediment supply are characterized by the development of an erosional surface over the pre-growth strata at the crest of the structure and an offlap pattern at the limbs. A more thorough discussion about the stratigraphic response and the evolution of topography in terms of these and other parameters is presented in the discussion section below.

6. Discussion

6.1. Initial assumptions and boundary conditions

Two critical assumptions were made during the derivation of the model. The first one is concerned with rocks having constant density. Many studies about the structure of active basins show that density increases with burial depth due to the closing of pore space as the overburden intensifies. Sediments can loose up to 60% of their volume by means of this mechanism during the first 3 km of burial, increasing their density from ~2000 kg/m^3 to ~2600 kg/m^3 (Allen and Allen, 2005). Clearly this effect is not small. The following is a linearized equation that includes the effects of compaction.

$$\frac{\partial V_X}{\partial X} + \frac{\partial V_Y}{\partial Y} + \epsilon V_Y = 0, \tag{22}$$

where ϵ is the ratio between the density gradient and surficial density ($\nabla\rho/\rho_0$). Using the values for these parameters discussed above, ϵ turns out to be a small constant in the order of 10^{-5} m^{-1}. Therefore, the model presented here should capture reasonably well the behavior of detachment folding, even if there are considerable changes in density with depth.

The second assumption made in the derivation is that the region deforms by buckling following a cosine function, a deformation mechanism characteristic of layered composite materials (Biot, 1961). The rheology of the material, however, is not considered explicitly in the model, for that it is necessary to incorporate the equation of balance of momentum and the constitutive relationship of the rocks. In spite of that, it can be demonstrated that the rheology of the material is implicitly contained in the boundary conditions. It becomes apparent for the limiting case of small axial strain, in which case the deformation function converges to the solution found by Biot (1961) for the buckling of a plate with an

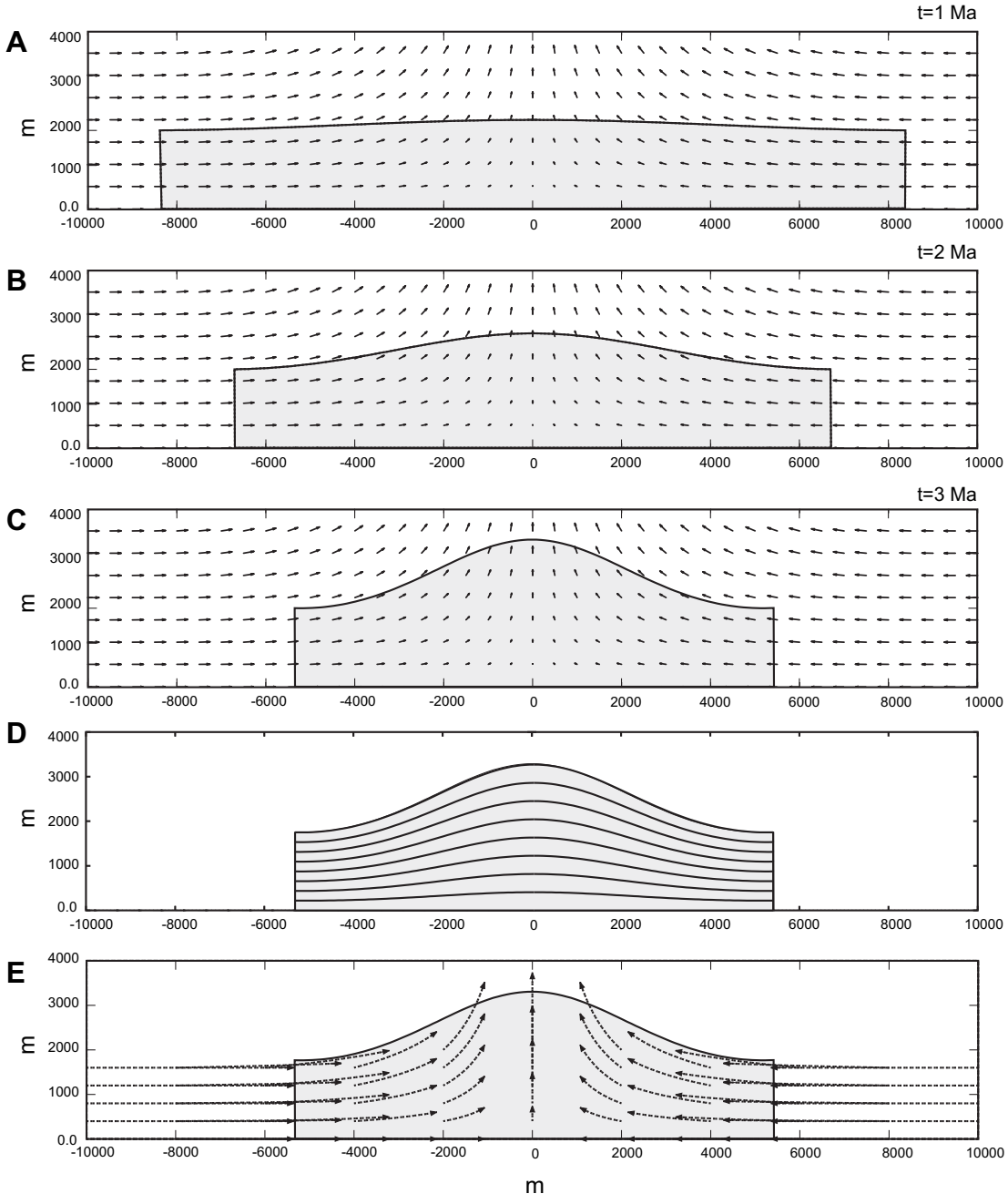

Fig. 5. Development of a detachment fold predicted by the model. The geometric and kinematic parameters are provided in the text. (A)–(C) Progression of folding as the medium shortens and moves through the Eulerian stationary velocity field depicted by the arrows. (D) Plot of internal deformation. (E) Plot of pathlines described by the material particles.

elastic–plastic composite structure (see Appendix B for further details).

6.2. Comparison of model predictions with seismic and experimental observations

The model has several of the features of the constant-area detachment fold models of Epard and Groshong (1993) and Epard and Groshong (1995). As in the case of these models, fold growth is achieved by changes in bed thickness, bed length, and rigid body rotation, while maintaining the hinges fixed and the depth of the detachment constant. However, the model derived here is based on continuous and smooth functions that result in significant differences. They produce, for example, a folded geometry similar to a Gaussian distribution curve, but with a shorter tail. This geometry is governed by the *Y*-component of the deformation function (Eq. (12)) in which the cosine function that modulates the vertical mass flux appears inside an exponential term.

Another difference is that this being a fully kinematic model, it can be established as to how the fold growth mechanisms evolve through time (see Appendix A for details and Fig. 8). Initially changes in bed thickness dominate acting over time as e^t. As time increases, changes in bed length by simple shear and rigid body rotations start to accommodate deformation, becoming the dominant mechanisms for large times as they operate as te^t. When combined they cause fold amplitude to grow exponentially with

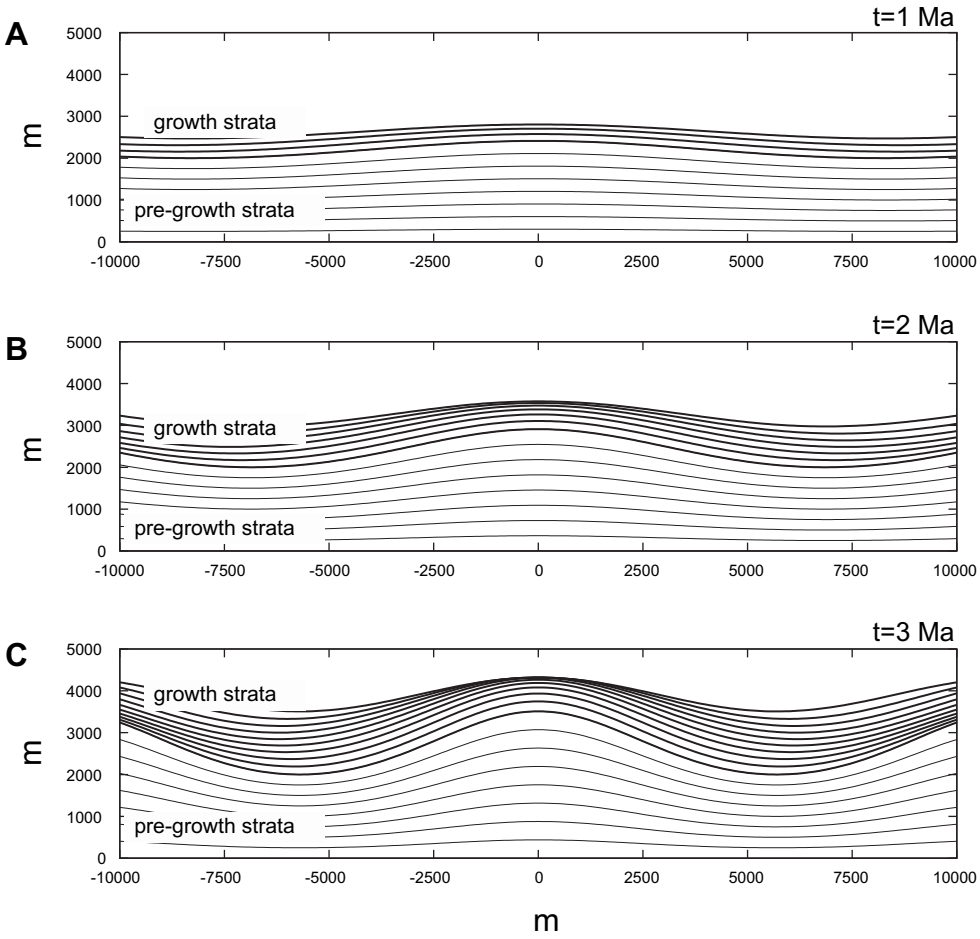

Fig. 6. Evolution of topography and growth strata predicted by the model. There are two sources of sediments in this solution. Sediments derived locally by mass diffusion and sediments from external sources that settle at a constant sedimentation rate. The simulation spans 3 Ma. See text for further details.

time, which is in agreement with other theoretical models of fold growth (Biot, 1961) and observations (Jackson and Talbot, 1986; Vergés et al., 1996; Daëron et al., 2007).

Shortening, on the other hand, has a reciprocal relation to fold growth decaying exponentially with time. Thus, it becomes increasingly difficult to compress the region as time increases. Naturally, the scaling factors have a similar relationship $\lambda_x = 1/\lambda_y$ (Eqs. (16) and (17)). For this reason, the model is not self-similar, i.e., a fold in a lower state of strain is not a scaled-down version of another one at a higher state of strain as Fig. 5A–C clearly shows. Instead, the model falls in the broader category of *self-affine* transformations in which an object is transformed unequally in different directions.

To test some of the previous results I made a cursory compilation of symmetrical low amplitude detachment folds around the world of different age, sedimentary environment, wavelength L, structural relief R, thickness H, and shortening u (Table 1). From this dataset, well-resolved continuous seismic reflectors within the pre-growth strata were digitized, normalized by their amplitude and half wavelengths, and then were compared against expression (12). Fig. 9A shows that the model fits reasonably well the loci of the normalized horizons regardless of their age, composition, and sedimentary environment, revealing that low amplitude detachment folds share a common profile. Fig. 9B is a log–log plot of the scaling factors λ_x and λ_y of eight of these detachment folds for which L, u, R and H can be reliably estimated. The scaling factors were estimated by means of the relations $\lambda_x = (L - u/2)/L$ and $\lambda_y = (H + R)/R$. Note that these quantities are non-dimensional and scale invariant. Therefore, any stratum can be used in their calculations because all parts of the system are scaled the same. The graph illustrates that an inverse relation (dashed line) fits, in the manner predicted by the model, the tendency of the data.

Numerous authors have documented the following property of detachment folds. A plot of the excess area A_e for several stratigraphic horizons vs. the depth to their undeformed stratigraphic level often results in a straight line. This is an important property because it can be used to constrain the depth-to-detachment in thrustbelts (Epard and Groshong, 1993; Bulmes and Poblet, 1999; Mitra, 2003; Scharer et al., 2004; González-Mieres and Suppe, 2006). This geometrical relationship is contained in the model derived here from first principles. In Eq. (14), the y term in the structural excess area can be factored out of the integral because integration is carried along the x-axis. Using expression (15), the structural excess area can then be expressed as $A_e = yu$, a function that is linear in y, the undeformed stratigraphic level.

In the model, detachment folds grow by the thickening of beds. As a consequence the structural relief R of internal beds also follows a relation $R \sim y$ as A_e does (Eq. (13)). In this regard, Wiltschko and Chapple (1977), Epard and Groshong (1993), and Hubert-Ferrari et al. (2007) documented naturally occurring structures that behave in this manner. Examples displaying this relationship are the Anjihad and the Yaken detachment folds located at the

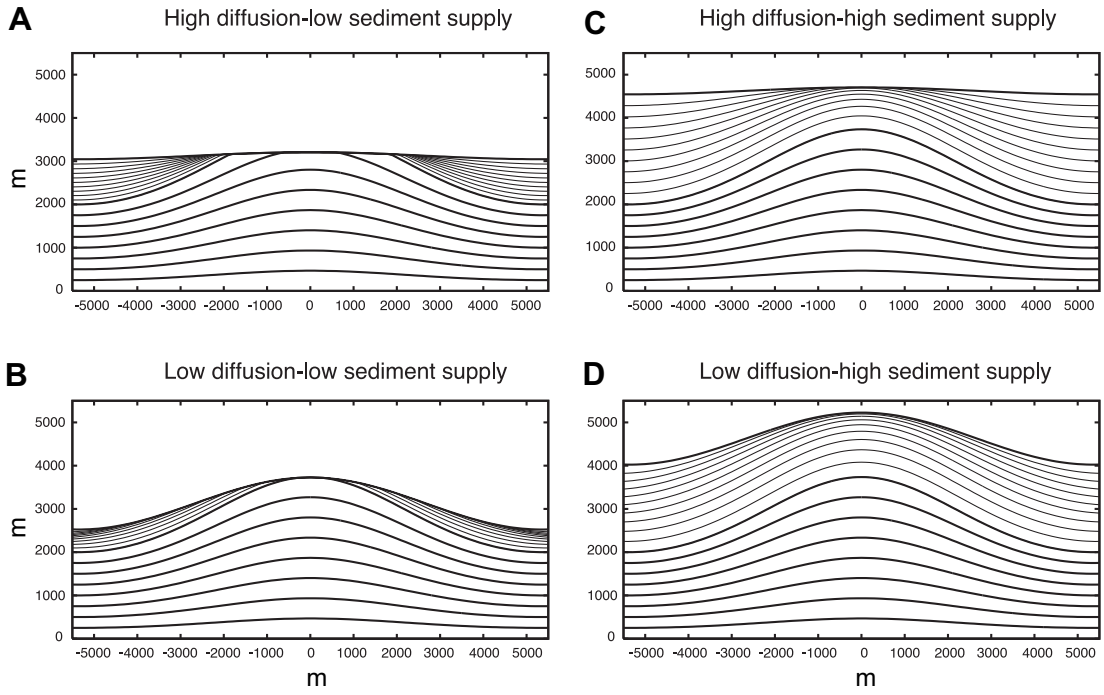

Fig. 7. Examples of growth strata patterns generated by the model. The solutions in the upper row are dominated by high erosion rates, whereas the solutions in the lower row are dominated by uplift. The column on the left corresponds to sediment starved basins; the column on the right corresponds to environments with a high sediment supply. See text for further details about the parameters used in these solutions.

piedmont of the Tian Shan Mountains in central Asia (Fig. 10). A graph of the structural relief vs. the height of the stratigraphic level above the detachment surface for several reflectors in these structures shows that a linear regression fits with little dispersion the trend delineated by the empirical data. Note, however, that the fit through the Yakeng detachment fold data does not intersect the origin as expression (12) predicts. A possible explanation for this, provided by Hubert-Ferrari et al. (2007), is that the fold underwent additional diapiric flow of salt at its base.

Measurements in sandbox experiments by Bernard et al. (2007) show that the Lagrangian velocity components of fault-related folds have relatively simple spatial patterns. They also found that deformation describes a progression starting with a stage of detachment tip folding that lasts up to $u \sim H/10$; this stage is followed by strain localization along a frontal fault that results in fault-bend folding. Fig. 11 presents a comparison between the measurements in the analog experiments by Bernard et al. (2007) and the Lagrangian velocity predicted by Eqs. (18) and (19). The figure consists of two stacked plots of the velocity components made along a vertical section that reveal how this physical field changes with height above the basal detachment. The horizontal velocity component of the model decreases linearly with distance toward the core of the fold. It reproduces the trend of the data up to a kink band that the experiment develops. Beyond the kink band, the correlation breaks down because the sand particles remain stationary. As for the vertical velocity component, it can be seen that the model reproduces the wavelength of the experimental fold, and the trend in amplitude change along the vertical direction. The uplift rate increases linearly with elevation above detachment, a relation that is also built in into the model (see Eq. (19), and Bernard et al., 2007, Fig. 9). However, fold wavelength in the experiment does not remain constant; it increases with height above the detachment surface, a feature that this analytical model cannot reproduce.

6.3. Topographic evolution and stratal pattern

Previously, it was shown how the mass diffusion coefficient and external sediment sources of sediments control the development of growth strata patterns and topography. We will further investigate what other parameters affect these processes. We will see that the rate of tectonic uplift and the initial geometry of the folded region also play a role on this.

The equation describing the topographic evolution (20) can be expressed in non-dimensional form in the following way (see Appendix C for details):

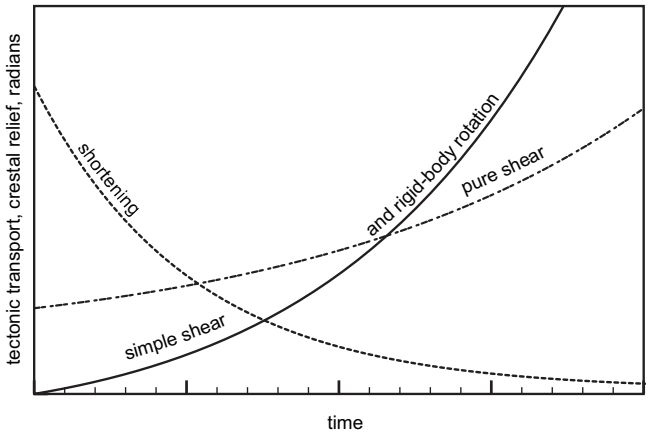

Fig. 8. Diagram showing how deformation is partitioned through time in the detachment model presented here. Initially, thickening of beds by pure shear dominates fold growth whereas in later stages growth is achieved predominantly by simple shear and rigid body rotation. At the same time, shortening decays exponentially with time.

Table 1
Compilation of symmetrical, low amplitude detachment folds observed in seismic cross-section in thrust belts around the world.

Location	Age of rocks	Age of folding	Sedimentary environment	L (km)	R (km)	H (km)	$u/2$ (km)	Reference
Southern North Sea	Paleozoic–Early Tertiary	Mid-Tertiary	Continental–Marine	11.5	1.0	0.8	4.5	Hughes and Davison (1993), Fig. 3
				16.4	0.8	0.4	7.6	Glennie (1998), Fig. 6.20
Tian Shan Piedmont, Central Asia	Late Miocene–present	Quaternary	Continental	7.69	0.75	3.25	0.69	Daëron et al. (2007), Fig. 14
				7.6	0.5	2.3[b]	0.6	Hubert-Ferrari et al. (2007), Fig. 6
Santos and Campos basin, Offshore Brazil	Cretaceous–present	Albian–present	Continental–Marine	20.0	1.2[a]	0.9[a]	7.6	Demercian et al. (1993), Fig. 5
Perdido fold belt, Gulf of Mexico	Jurassic–present	Eocene–present	Marine	–	2[a]	–	–	Trudgill et al. (1999), Fig. 12
Angola continental slope, SW Africa	–	–	–	3.5	0.95	1.8	0.5	Shaw et al. (2005), p. 38
Zagros fold belt, Middle East	Paleozoic–Cenozoic	Cenozoic	Carbonate platform	–	0.3[a]	8.2[a]	–	Sherkati et al. (2005), Fig. 5
Wyoming thrust belt, North America	–	–	–	4.85	0.53	2.8	0.35	Groshong and Epard (1993), Fig. 10
Appalachian fold belt, North America	Sillurian–Devonian	Pennsylvanian–Permian	Carbonate platform	10.78	0.79	0.12	0.08	Wiltschko and Chapple (1977), Fig. 3

L is half the wavelength of the fold, R is the structural relief of a well-imaged reflector within the pre-growth strata, H is the height above the detachment surface of the reflector in its undeformed position, and u is the tectonic transport along the basal detachment.
[a] Based on a seismic wave propagation velocity of 2000 m/s.
[b] Average thickness.

$$\eta = \gamma Pe\left(1 - e^{-t/2\tau_d}\right)\cos(X/\ell) + \frac{t}{\tau_t} + \frac{t}{\tau_s}, \tag{23}$$

where η is the normalized change in topographic relief, γ is the aspect ratio of the region, $\ell = L/\pi$ is the characteristic wavelength of the fold, Pe is the Péclet number, a non-dimensional quantity given by the ratio between the mass flux due to tectonic uplift and the diffusion of mass by erosion and sedimentation, τ_d is the characteristic time at which diffusion takes place, and τ_t and τ_s are characteristic times associated with tectonic uplift and sedimentation, respectively. From this last equation, it can be seen that for t in excess of $3\tau_d$, the term $e^{-t/2\tau_d}$ becomes negligible and the topography reaches a steady state with a constant amplitude dictated by γPe (Fig. 12)

$$\eta = \gamma Pe\cos(X/\ell) + \frac{t}{\tau_t} + \frac{t}{\tau_s}. \tag{24}$$

Thus, low values of γPe will result in a flat topography as in solutions A and C in Fig. 7, whereas high values of γPe will produce an emerging detachment fold as in solutions B and C in Fig. 7. From Eq. (24) it can also be demonstrated that for $\tau_s^{-1} > \gamma Pe/2\tau_d = v_u/2H$ sedimentation predominates over erosion and uplift, which will result in a covered anticline (see Appendix C for further details). Note, however, that from Eq. (12) the structural relief grows with time as e^t. If sedimentation rate remains constant through time, as in the model presented here, then uplift will eventually surpass accumulation of sediments resulting in a thinning-upward pattern

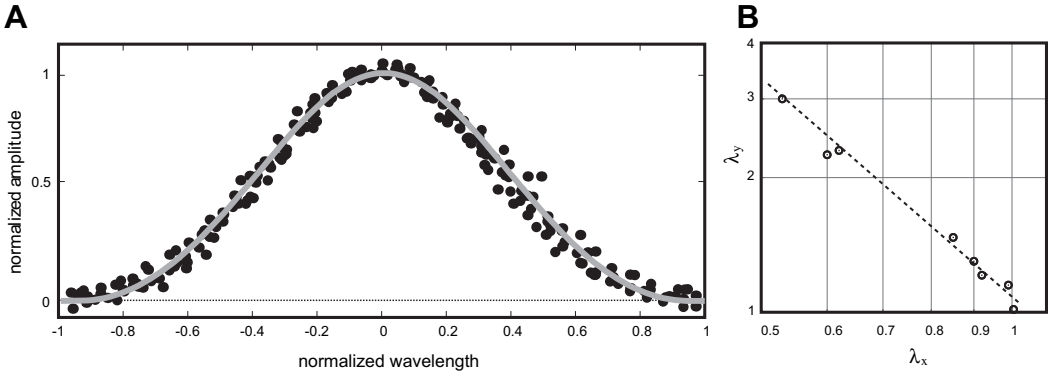

Fig. 9. A) Comparison of the fold geometry predicted by the model (gray line) with the geometry of actual detachment folds listed in Table 1 (dots). Log–log plot of the scaling factors for eight of the detachment folds listed in Table 1. Dotted line corresponds to the best fit function of the form $y = A/x$, where $A = 1.25$.

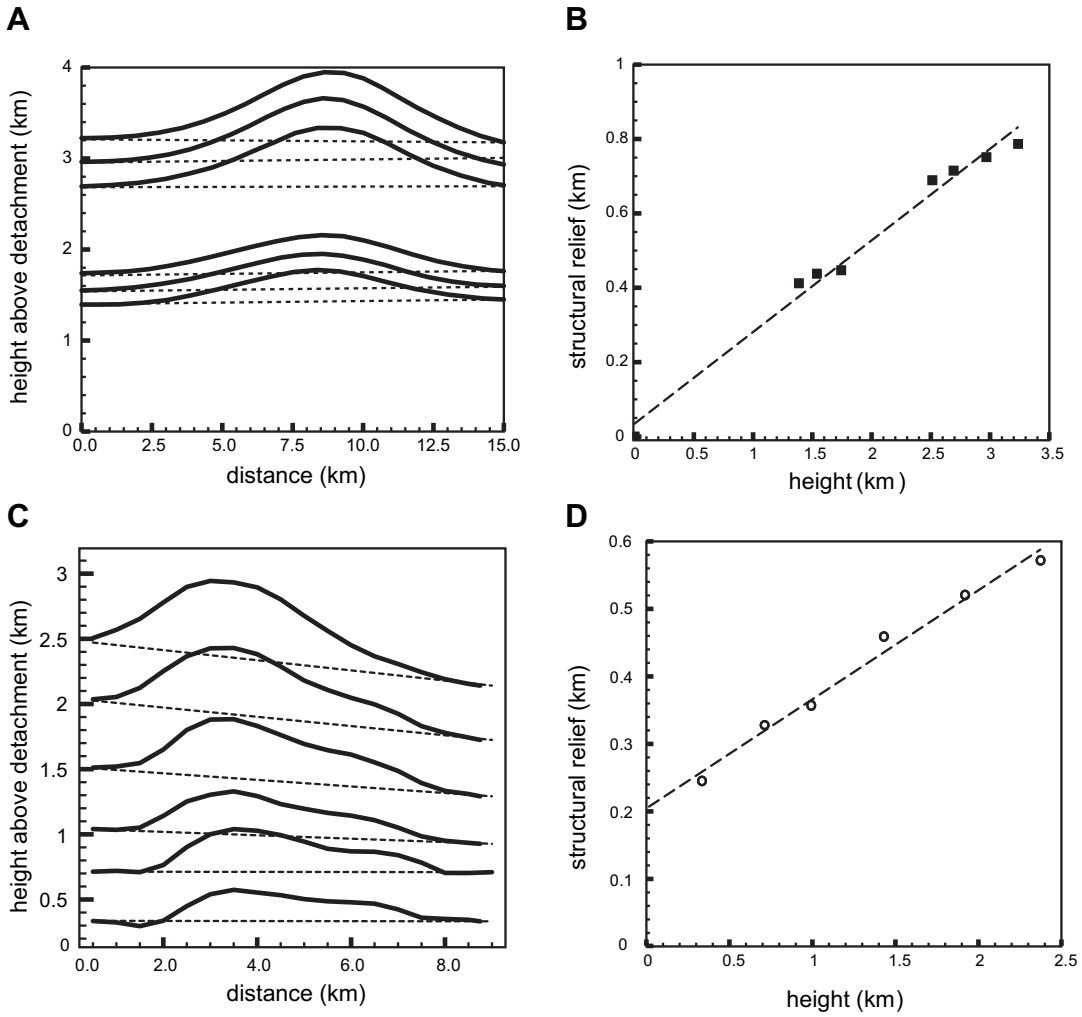

Fig. 10. A) Digitized stratigraphic horizons of the Anjihai detachment fold in the northern Tian Shan Piedmont citepDeatl2007. (B) Plot of structural relief vs. height above detachment of the original stratigraphic level for the stratigraphic horizons of the Anjihai detachment fold. (C) Digitized stratigraphic horizons of the Yakeng detachment fold in the southern Tian Shan Piedmont (González-Mieres and Suppe, 2006; Hubert-Ferrari et al., 2007). (D) Plot of structural relief vs. height above detachment of the original stratigraphic level for the stratigraphic horizons of the Yakeng detachment fold.

in timelines and the development of a strong unconformity at the crest of the fold.

I selected a detachment fold from the North Sea salt pillows to test the detachment folding and stratal growth patterns predicted by the model (Fig. 13A). The rocks involved in the deformation consist of a basal layer of evaporites of Permian age, overlain by a thick sequence of competent clastic continental rocks and marine carbonates of Mesozoic age. During the early

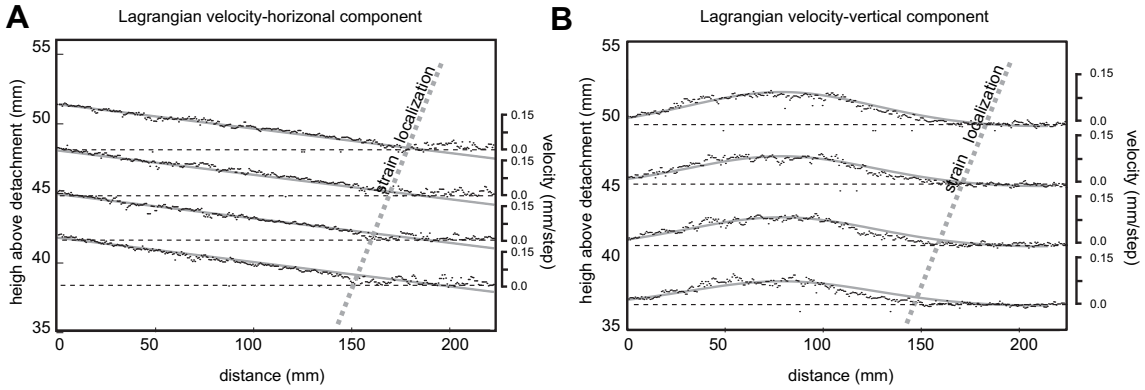

Fig. 11. Comparison of the Lagrangian velocity components predicted by the model (solid lines) with velocity profiles (dots) from measurements in sandbox experiments by Daëron et al. (2007). (A) Comparison for the *x*-component. (B) Comparison for the *y*-component.

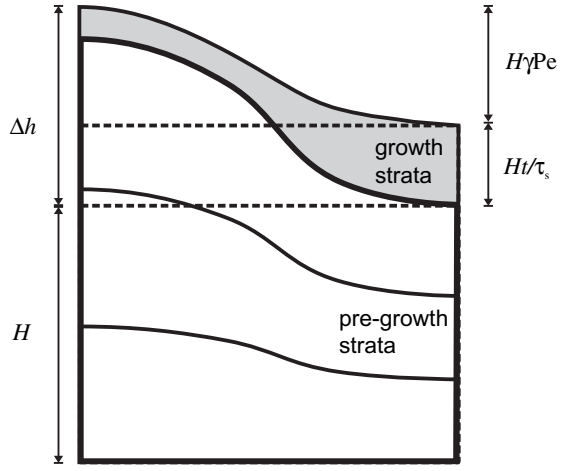

Fig. 12. Sketch showing the geometrical meaning of the various non-dimensional quantities that appear in the solution of the growth strata model: Δh is the change in topography due to folding, erosion, and sedimentation; γ is the aspect ratio of the region; Pe is the Péclet Number, the ratio between the flux due to tectonic uplift and the mass flux by erosion and sedimentation; τ_s is a characteristic time in which sedimentation takes place. Further details are provided in the text and Fig. 3.

Tertiary this sequence was folded by a small phase of localized inversion that gave rise to detachment folds throughout the area, disrupting the sedimentation of a sequence of predominantly clastic sediments.

This detachment fold contains units with contrasting mechanical properties and its development cannot be simulated with the model because it assumes a homogenous lithology. To deal with this complexity, I considered a two-layer model in which the ductile basal unit (purple unit in Fig. 13) deforms by parallel-to-bed pure shear, whereas the competent units (cyan unit) deform by similar folding (vertical simple shear). Given the low amplitude of the fold, the later mode of folding is a good approximation to the way in which competent units deform by concentric parallel folding.

The geometrical and non-dimensional parameters needed to simulate the deformation and accumulation of growth strata of this detachment fold can be estimated directly from the seismic cross-section (see also the first row of values in Table 1); it can be seen that γPe is a small number in the order of 0.01 or less because the structure lacks relief; $L = 11.5$ km, and $H = 0.8$ km; that places $\gamma = 4.5$. A simple algebraic manipulation involving these quantities constrains some of their ratios: $\mathrm{Pe} = 2 \times 10^{-3}$, $v_u/\kappa = 6 \times 10^{-7}$ m, and $\dot{s}/\kappa < 6 \times 10^{-7}$ m. In other words, the rate of erosion significantly exceeded those of sedimentation and uplift. Fig. 13B shows the simulated structure and stratigraphy of the North Sea detachment fold. The model reproduces the first-order features of the geometry and stratigraphic relations observed in the fold. Note how the model captures accurately the fold shape in which synclines are broader than the central anticline, a feature that a simple periodic function (i.e., sine or cosine functions) cannot recreate. Also note the development of a progressive unconformity at the fold limbs and crest of the central anticline. However, artifices in the seismic imaging make a detailed comparison between model and data difficult. This is especially true at the limbs of the structure, where multiple reflections obscure stratigraphic relations.

7. Conclusions

I have presented a simple model for the evolution of low amplitude detachment folding that satisfies the conservation of mass principle. Unlike previous models that have highly idealized geometries in which folds are straight-limbed and sharp hinged, the model presented here is smooth and strain is accommodated continuously. The geometry predicted by the model is close to that of a Gaussian distribution function in which fold wavelength remains constant with depth, resulting in similar folding.

This paper also presented a model for growth strata built upon the detachment folding model. It is important to reproduce these stratigraphic features because they impose stringent constraints on the kinematics of deformation. The model uses the transport-diffusion equation to simulate the effects of erosion,

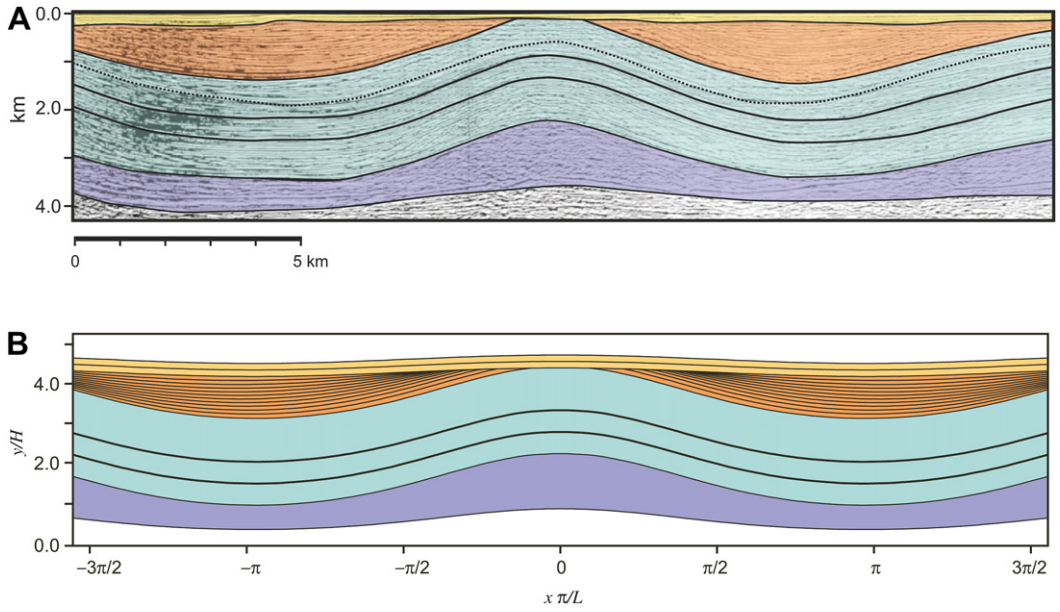

Fig. 13. A) Seismic cross-section of a detachment fold in the southern North Sea. Blue area corresponds to a ductile layer of salt; green sequences correspond to competent Mesozoic continental and marine rocks; orange sequence corresponds to syntectonic strata of late Tertiary age. (B) Simulation of the evolution of detachment folding and growth strata for the structure illustrated in (A). The model uses the following parameters: $\mathrm{Pe} = 2 \times 10^{-3}$, $v_u/\kappa = 6 \times 10^{-7}$ m, and $\dot{s}/\kappa = 4 \times 10^{-7}$ m, and $\gamma = 4.5$. See text for further details.

sedimentation, and deposition of sediments from distant sources. These processes can be characterized in terms of non-dimensional quantities and characteristic times. These include the Péclet number, the aspect ratio of the region, and the characteristic times associated with the rate of tectonic uplift and sedimentation. The models display the following geometrical and kinematic properties:

1 Folding is a highly unstable process in which structural relief grows exponentially with time when the contraction rate is constant.
2 The core of the fold grows by parallel-to-bed pure shear that results in changes in thickness and longitude in beds across the fold.
3 The structural relief and excess area increase in linear proportion with elevation above the basal detachment.
4 Folding is a self-affine process. As deformation progresses the resulting fold is not a scaled version of itself, instead, the shape is strained by different scaling factors along the horizontal and vertical direction. The factors have a reciprocal relation to conserve mass in the fold.
5 Growth strata exhibit progressive unconformities and form fanning patterns of sedimentary sequences on the limbs of the fold.
6 The dip of syntectonic strata increases with age, i.e., older sediments dip more steeply than do younger sediments.

All these features are in agreement with geometric, and stratigraphic relations documented in fold-and-thrust belts, and analog experiments.

Acknowledgments

I am grateful to my colleagues of CICESE's applied seismology group for helpful comments received during the development of the ideas presented in this paper. I am also grateful to Juán García-Abdeslem, Max Suter, Greg Hirth, and two anonymous reviewers whose comments substantially improved the paper. José de Jesús Mojarro-Bermúdez and Luis Carlos Gradilla Martínez provided technical support to the author. This work was funded by a grant from the Mexican Council of Science (CONACyT grant no. 60647) and by CICESE (project no. 644116).

Appendix A. Detachment folding model

The boundary value problem (BVP) used here to describe detachment folding is the following:

$$\frac{\partial V_X}{\partial X}+\frac{\partial V_Y}{\partial Y}=0, \tag{A.1}$$

$$V_X(0,Y)=0, \tag{A.2}$$

$$V_X(L,Y)=v_s, \tag{A.3}$$

$$V_Y(X,0)=0, \tag{A.4}$$

$$V_Y(L,Y)=0, \tag{A.5}$$

$$V_Y(X,H)=\frac{v_u}{2}\cos(\pi X/L)+\frac{v_u}{2}. \tag{A.6}$$

One strategy to solve this homogeneous partial differential equation with non-homogenous boundary conditions (BC) is to assume that v_Y can be expressed as the product of two independent functions of X and Y

$$V_Y=\alpha(X)\beta(Y), \tag{A.7}$$

and from Eq. (A.1), V_X can be expressed as

$$\frac{\partial V_X}{\partial X}=-\alpha(X)\frac{\mathrm{d}\beta(Y)}{\mathrm{d}Y}. \tag{A.8}$$

The next step is to calculate the integral of this last expression to find the flux leaving an arbitrary region $(0, X)\times(0, Y)$

$$\int_0^Y\int_0^X\frac{\partial V_X}{\partial X}\,\mathrm{d}Y\,\mathrm{d}X=\int_0^Y\int_0^X\alpha(X)\frac{\mathrm{d}\beta Y}{\mathrm{d}Y}\,\mathrm{d}Y\,\mathrm{d}X. \tag{A.9}$$

Using BC (A.2), this integral simplifies to the following expression:

$$\int_0^Y V_X\,\mathrm{d}Y=A(X)\beta(Y), \tag{A.10}$$

where $A(X)=\int\alpha(X)\,\mathrm{d}X$. By evaluating this expression at $X=L$ and using BC (A.3)

$$v_sY=A(L)\beta(Y). \tag{A.11}$$

It can be seen that $\beta(Y)$ must be a linear function of Y. The same reasoning can be used to infer the form of $\alpha(X)$ using BC (A.6); clearly, $\alpha(X)=v_u/2\cos(\pi X/L)+v_u/2$. Combining those two results, the vertical component of the velocity field is

$$V_Y=\frac{v_uY}{2H}\cos(\pi X/L)+\frac{v_uY}{2H}. \tag{A.12}$$

Finally, from Eqs. (A.12) and (A.8) it is a straightforward procedure to derive

$$V_X=-\frac{Lv_u}{2\pi H}\sin(\pi X/L)-\frac{v_uX}{2H}, \tag{A.13}$$

Now, the pathlines are the family of curves $\boldsymbol{\sigma}(t)$ that satisfy the following system of differential equations:

$$\sigma_X'(t)=V_X(\sigma_Y(t),\,t), \tag{A.14}$$

$$\sigma_Y'(t)=V_Y(\sigma_Y(t),\,t). \tag{A.15}$$

Upon substitution of Eqs. (A.13) and (A.12) in (A.14) and (A.15)

$$\sigma_X'(t)=-\frac{Lv_u}{2\pi H}\sin(\pi\sigma_X/L)-\frac{v_u\sigma_X}{2H}, \tag{A.16}$$

$$\sigma_Y'(t)=\frac{v_u\sigma_Y}{2H}\cos(\pi X/L)+\frac{\sigma_Y}{2H}. \tag{A.17}$$

Rearranging terms

$$\frac{\mathrm{d}\sigma_X}{\frac{L}{\pi}\sin(\pi\sigma_X/L)+\sigma_X}=-\frac{v_u}{2H}\,\mathrm{d}t, \tag{A.18}$$

$$\frac{\mathrm{d}\sigma_Y}{\sigma_Y}=\left(\frac{v_u}{2H}\cos(\pi X/L)+\frac{1}{2H}\right)\mathrm{d}t. \tag{A.19}$$

Expression (A.18) is quite cumbersome and probably does not have a closed-form solution. An approximate solution can be found by performing a truncated Taylor's expansion to the first term of the sine function, in which case the left-hand side of expression (A.18)

reduces to the more manageable form $d\sigma_X/2\sigma_X$. The approximate solution is given by the expressions:

$$\sigma_X = \sigma_X^0 e^{-t\nu_u/H}, \tag{A.20}$$

$$\sigma_Y = \sigma_Y^0 e^{t\nu_u[\cos(\pi X/L)+1]/2H}. \tag{A.21}$$

σ_X^0 and σ_Y^0 correspond with the material positions of particles (x, y) in the undeformed state at $t = 0$, and σ_X and σ_Y with the spatial positions (X, Y) of particles in the deformed state.

$$X = xe^{-t\nu_u/H}, \tag{A.22}$$

$$Y = ye^{t\nu_u[\cos(\pi x/L)+1]/2H}. \tag{A.23}$$

These two last equations are the deformation function f of the detachment folding process. From them the infinitesimal strain tensor, $\boldsymbol{E} = \frac{1}{2}(\nabla f + \nabla f^T)$, and the infinitesimal rotation tensor, $\boldsymbol{W} = \frac{1}{2}(\nabla f - \nabla f^T)$, can be obtained.

$$\boldsymbol{E} = \begin{pmatrix} e^{-t\nu_u/H} & \frac{\pi\nu_u y}{4HL}\sin\left(\frac{\pi x}{L}\right)te^{t\nu_u[\cos(\pi x/L)+1]/2H} \\ \frac{\pi\nu_u y}{4HL}\sin\left(\frac{\pi x}{L}\right)te^{t\nu_u[\cos(\pi x/L)+1]/2H} & e^{t\nu_u[\cos(\pi x/L)+1]/2H} \end{pmatrix}, \tag{A.24}$$

$$\boldsymbol{W} = \begin{pmatrix} 0 & -\frac{\pi\nu_u y}{4HL}\sin\left(\frac{\pi x}{L}\right)te^{t\nu_u[\cos(\pi x/L)+1]/2H} \\ \frac{\pi\nu_u y}{4HL}\sin\left(\frac{\pi x}{L}\right)te^{t\nu_u[\cos(\pi x/L)+1]/2H} & 0 \end{pmatrix}. \tag{A.25}$$

Therefore, the deformation process is accomplished by contractions and dilations (diagonal terms in $\boldsymbol{E}$), simple shear (off-diagonal terms in $\boldsymbol{E}$) and rigid body rotations given by $\boldsymbol{W}$.

Appendix B. Convergence to Biot's solution to the problem of the buckling of an elastic plate embedded in a viscous fluid

The solution of Biot (1961) to this classical problem is given by

$$\omega = \omega_0 \cos(2\pi x/\lambda)e^{t/\tau}, \tag{B.1}$$

where ω is the deflection of the plate, λ is the wavelength of the folding, and τ is a characteristic time that controls how fast the buckling instability grows. These two parameters depend on the elastic parameters of the plate, its thickness, and viscosity of the fluid. For the limiting case of small axial strains the displacement field is given by

$$u_x = X - x \approx 0 \tag{B.2}$$

$$u_y = Y - y = ye^{\nu_u t\,\cos(\pi X/L)/2H}e^{t\nu_u/2H} - y \tag{B.3}$$

Note that the exponential term of the vertical deformation component is split into two parts: one containing a spatial term only and another one containing a temporal term only. If the spatial term is small then it can be replaced by Taylor's expansion linearizing that term. Then Eq. (B.3) reduces to

$$\omega \approx u_y = \frac{y\nu_u t}{2H}\cos(\pi x/L)e^{t\nu_u/2H} - y. \tag{B.4}$$

By setting $y\nu_u t/2H = \omega_0$, $L/2 = \lambda$, and $2H/\nu_u = \tau$ expression (B.1) is recovered.

Appendix C. Erosion and sedimentation model

The transport-diffusion equation (6) is used here to model erosion and sedimentation synchronous with detachment folding. However, to solve this equation, further simplifications are required. Firstly, I will assume that the product of the topographic gradient with the horizontal velocity component $V_X\partial h/\partial X$ is negligible, given the low amplitude of the detachment fold and the slow deformation rate involved in the problem. Secondly, V_Y is evaluated in $Y = H$ to describe the tectonic uplift rate at the top of the region. Thirdly, reflective boundary conditions are imposed at the ends of the region; therefore, the net flux of mass leaving it as zero. Another way to see these last boundary conditions is that the detachment fold being modeled is part of a group of congruent folds and the outbound flux of mass cancels out by an inbound flux from adjacent folds. The initial conditions and boundary value problem that describe the degradation of topography is

$$\frac{\partial h}{\partial t} = -\kappa\frac{\partial^2 h}{\partial X^2} - \frac{\nu_u}{2}\cos(\pi X/L) - \nu_u/2 + \dot{s}, \tag{C.1}$$

$$h = H, \quad t = 0, \tag{C.2}$$

$$\frac{\partial h}{\partial X} = 0, \quad X = 0, L. \tag{C.3}$$

The solution to this problem can be found in numerous textbooks e.g., Farlow (1993)

$$h = \frac{\nu_u L^2}{\kappa\pi^2}\left(1 - e^{-t\kappa\pi^2/2L^2}\right)\cos(\pi X/L) + \frac{t\nu_u}{2} + \dot{s}t + H. \tag{C.4}$$

This expression can be rearranged in the following way

$$\frac{h-H}{H} = \frac{L}{\pi H}\frac{\nu_u L}{\kappa\pi}\left(1 - e^{-t\kappa\pi^2/2L^2}\right)\cos(\pi X/L) + \frac{\nu_u}{2H}t + \frac{\dot{s}}{H}t. \tag{C.5}$$

Now, when the following characteristic length $\ell = L/\pi$ and characteristic times $\tau_t = 2H/\nu_u$, $\tau_s = H/\dot{s}$, and $\tau_d = \ell^2/\kappa$ are introduced, Eq. (C.5) can expressed as

$$\frac{h-H}{H} = \frac{\ell}{H}\frac{\nu_u\ell}{\kappa}\left(1 - e^{-t/2\tau_d}\right)\cos(X/\ell) + \frac{t}{\tau_t} + \frac{t}{\tau_s}. \tag{C.6}$$

The left-hand side of this equation is the normalized change in topographic relief, whereas the ratio ℓ/H on the right-hand side of the equation can be considered as the aspect ratio of the region; furthermore the non-dimensional quantity $\nu_u\ell/\kappa$ is the Péclet number. By denoting these three non-dimensional quantities as η, γ, and Pe, the previous expression simplifies to

$$\eta = \gamma Pe\left(1 - e^{-t/2\tau_d}\right)\cos(X/\ell) + \frac{t}{\tau_t} + \frac{t}{\tau_s}. \tag{C.7}$$

By differentiating with respect to time one can obtain the rate at which erosion and sedimentation proceed

$$\frac{\partial\eta}{\partial t} = \frac{\gamma Pe}{2\tau_d}e^{-t/2\tau_d}\cos(X/\ell) + \frac{1}{\tau_t} + \frac{1}{\tau_s}. \tag{C.8}$$

From this result, it can be appreciated that if

$$\frac{1}{\tau_s} > \frac{\gamma Pe}{2\tau_d}, \tag{C.9}$$

then sedimentation predominates over erosion. Finally, by substituting the values of $Pe = v_u \ell/\kappa$, and $\tau_d = \ell^2/\kappa$, we obtain

$$\frac{1}{\tau_s} > \frac{v_u}{2H}. \quad (C.10)$$

References

Allen, P.A., Allen, J.R., 2005. Basin Analysis Principles and Applications, second ed. Oxford Blackwell Publishing.

Bernard, S., Avouac, J.P., Dominguez, S., Simoes, M., 2007. Kinematics of fault-related folding derived from a sandbox experiment. Journal of Geophysical Research 112, B03S12. doi:10.1029/2005JB004149.

Biot, M.A., 1961. Theory of folding of stratified visco-elastic media and its implications in tectonics and orogenesis. Geological Society of America Bulletin 72, 1595–1620.

Bulmes, M., Poblet, J., 1999. Estimating the detachment depth in cross sections involving detachment folds. Geological Magazine 136, 395–412.

Carson, M.A., Kirkby, M.J., 1972. Hillslope Form and Process. Cambridge University Press, New York.

Cloetingh, S., Burov, E., Poliakov, A., 1999. Lithosphere folding: primary response to compression? (from central Asia to Paris basin). Tectonics 18, 1064–1083.

Contreras, J., Suter, M., 1990. Kinematic modeling of cross-sectional deformation sequences by computer simulation. Journal of Geophysical Research 95, 21913–21929.

Contreras, J., Suter, M., 1997. A kinematic model for the formation of duplex systems with a perfectly planar roof thrust. Journal of Structural Geology 19, 269–278.

Culling, W.E.H., 1963. Soil creep and the development of hillside slopes. Journal of Geology 71, 127–162.

Daëron, M., Avouac, J.P., Charreau, J., 2007. Modeling the shortening history of a fault tip fold using structural and geomorphic records of deformation. Journal of Geophysical Research 112, B03S13. doi:10.1029/2006JB004460.

den Bezemer, T., Kooi, H., Cloetingh, S., 1999. Numerical modeling of fault-related sedimentation. In: HarbaughJ., WatneyL., RankeyG., SlingerlandR., GoldsteinR., FranseenE. (Eds.), Numerical Experiments in Stratigraphy: Recent Advances in Stratigraphic and Sedimentologic Computer Simulations. SEPM Special Publication # 62,Tulsa, pp. 177–196.

Demercian, S., Szatmari, P., Cobbold, P.R., 1993. Style and pattern of salt diapirs due to thin-skinned gravitational gliding, Campos and Santos basins, offshore Brazil. Tectonophysics 228, 393–433.

Epard, J.L., Groshong Jr., R.H., 1995. Kinematic model of detachment folding including limb rotation, fixed hinges and layer-parallel strain. Tectonophysics 247, 85–103.

Epard, J.L., Groshong Jr., R.H., 1993. Excess area and depth to detachment. AAPG Bulletin 77, 1291–1302.

Farlow, S.J., 1993. Partial Differential Equations for Scientists and Engineers. Dover Publications Inc., New York.

Garcia-Castellanos, D., Vergés, J., Gaspar-Escribano, J., Cloetingh, S., 2003. Interplay between tectonics, climate, and fluvial transport during the Cenozoic evolution of the Ebro Basin (NE Iberia). Journal of Geophysical Research 108 (B7), 2347. doi:10.1029/2002JB002073.

Glennie, K.W., 1998. Petroleum Geology of the North Sea: Basic Concepts and Recent Advances, fourth ed. Blackwell.

González-Mieres, R., Suppe, J., 2006. Relief and shortening in detachment folds. Journal of Structural Geology 28, 1785–1807.

Hardy, S., 1995. A method for quantifying the kinematics of fault-bend folding. Journal of Structural Geology 17, 1785–1788.

Hardy, S., Poblet, J., McClay, K., Waltham, D., 1996. Mathematical modelling of growth strata associated with fault-related fold structures. In: Geological Society London Special Publications, vol. 99, pp. 265–282.

Hardy, S., Connors, C.D., 2006. Short note: a velocity description of shear fault-bend folding. Journal of Structural Geology 28, 536–543.

Hardy, S., Poblet, J., 1994. Geometric and numerical model of progressive limb rotation in detachment folds. Geology 22, 371–374.

Hardy, S., Poblet, J., 1995. The velocity description of deformation. Paper 2: sediment geometries associated with fault-bend and fault-propagation folds. Marine and Petroleum Geology 12, 165–176.

Hubert-Ferrari, A., Suppe, J., Gonzalez-Mieres, R., Wang, X., 2007. Mechanisms of active folding of the landscape (southern Tian Shan, China). Journal of Geophysical Research 112, B03S09. doi:10.1029/2006JB004362.

Hughes, M., Davison, I., 1993. Geometry and growth kinematics of salt pillows in the southern North Sea. Tectonophysics 228, 239–254.

Jackson, M.P.A., Talbot, C.J., 1986. External shapes, strain rates, and dynamics of salt structures. Geological Society of America Bulletin 97, 305–323.

Jamison, W.R., 1987. Geometric analysis of fold development in overthrust terranes. Journal of Structural Geology 9, 207–219.

Kwon, D.Y., Park, F.C., Chi, D.P., 2005. Inextensible flows of curves and developable surfaces. Applied Mathematics Letters 18, 1156–1162.

Landau, L.D., Lifshitz, E.M., 1987. Fluid Mechanics, second ed. Pergamon Press, Oxford.

Mial, A.D., 1997. The Geology of Stratigraphic Sequences. Springer, New York.

Mitra, S., 1990. Fault-propagation folds: geometry, kinematic evolution, and hydrocarbon traps. AAPG Bulletin 74 doi:10.1016/S0191-8141(02)00198-0.

Mitra, S., 2003. A unified kinematic model for the evolution of detachment folds. Journal of Structural Geology 25, 1659–1673.

Nash, D.B., 2005. A general method for morphologic dating of hillslopes. Geology 33, 693–695.

Nemčok, M., Schamel, S., Gayer, R., 2005. Thrustbelts Structural Architecture, Thermal Regimes, and Petroleum Systems. Cambridge University Press, New York.

Poblet, J., Hardy, S., 1995. Reverse modelling of detachment folds: application to the Pica de1 Aguila anticline in the South Central Pyrenees (Spain). Journal of Structural Geology 17, 1707–1724.

Poblet, J., McClay, K., 1996. Geometry and kinematics of single-layer detachment folds. AAPG Bulletin doi: 10.1306/64ED8CA0-1724-11D7-8645000102C1865D.

Poblet, J., McClay, K., Storti, F., Muñoz, J.A., 1997. Geometries of syntectonic sediments associated with single-layer detachment folds. Journal of Structural Geology 19, 369–381.

Poblet, J., Bulnes, M., McClay, K., Hardy, S., 2004. Plots of crestal structural relief and fold area versus shortening – a graphical technique to unravel the kinematics of thrust-related folds. In: McClay, K. (Ed.), Thrust Tectonics and Hydrocarbon Systems. AAPG Memoir 82. The American Association of Petroleum Geologists, Tulsa, pp. 372–399.

Scharer, K.M., Burbank, D.W., Chen, J., Weldon, R.J., Rubin, C., Zhao, R., Shen, J., 2004. Detachment folding in the Southwestern Tian Shan – Tarim foreland, China: shortening estimates and rates. Journal of Structural Geology 26, 2119–2137.

Scharer, K.M., Burbank, D.W., Chen, J., Weldon, R.J., 2006. Kinematic models of fluvial terraces over active detachment folds: constraints on the growth mechanism of the Kashi-Atushi fold system, Chinese Tian Shan. GSA Bulletin 118, 1006–1021.

Shaw, J.H., Connors, C.D., Suppe, J., 2005. Structural interpretation methods. In: Shaw, J.H., Connors, C.D., Suppe, J. (Eds.), Seismic Interpretation of Contractional Fault-Related Folds: AAPG Seismic Atlas. Studies in Geology #53. The American Association of Petroleum Geologists, Tulsa.

Sherkati, S., Molinaro, M., de Lamotte, D.F., Letouzey, J., 2005. Detachment folding in the Central and Eastern Zagros fold-belt (Iran): salt mobility, multiple detachments and late basement control. Journal of Structural Geology 27, 1680–1696.

Storti, F., Salvini, F., McClay, K., 1997. Fault-related folding in sandbox analogue models of thrust wedges. Journal of Structural Geology 19, 583–602.

Suppe, J., 1983. Geometry and kinematics of fault-bend folding. American Journal of Science 283, 684–721.

Suppe, J., 1985. Principles of Structural Geology. Prentice-Hall, Englewood Cliffs.

Suppe, J., Chou, G.T., Hook, S.C., 1992. Rates of folding and faulting determined from growth strata. In: McClay, K.R. (Ed.), Thrust Tectonics. Chapman & Hall, Suffolk, pp. 105–121.

Suppe, J., Medwedeff, D.A., 1990. Geometry and kinematics of fault-propagation folding. Eclogae Geologicae Helvetiae 83, 409–454.

Suppe, J., Sàbat, F., Muñoz, J.A., Poblet, J., Roca, E., Vergés, J., 1997. Bed-by-bed fold growth by kink-band migration: Sant llorenc de Morunys, eastern Pyrenees. Journal of Structural Geology, 443–461. doi: 10.1016/S0191-8141(96)00103-4.

Suppe, J., Connors, C.D., Zhang, Y., 2004. Shear fault-bend folding. In: McClay, K.R. (Ed.), Thrust Tectonics and Hydrocarbon Systems. AAPGMemoir82. The American Association of Petroleum Geologists, Tulsa, pp. 303–323.

Riba, O., 1976. Syntectonic unconformities of the Alto Cardener, Spanish Pyrinees: a genetic interpretation. Sedimentary Geology 15, 213–233.

Trudgill, B.D., Rowan, M.G., Fiduk, J.C., Weimer, P., Gale, P.E., Korn, B.E., Phair, R.L., Gafford, W.T., Roberts, G.R., Dobbs, S.W., 1999. The Perdido fold belt, northwestern deep Gulf of Mexico, part 1: structural geometry, evolution and regional implications. AAPG Bulletin 83, 88–113.

Vergés, J., Burbank, D.W., Meigs, A., 1996. Unfolding: an inverse approach to fold kinematics. Geology 24, 175–178.

Waltham, D., Hardy, S., 1995. The velocity description of deformation. Paper 1: theory. Marine and Petroleum Geology 12, 153–163.

Wilkerson, M.S., Wilson, J.M., Poblet, J., Fischer, M.P., 2004. DETACH: an Excel spreadsheet to simulate 2-D cross sections of detachment folds. Computers and Geosciences 30, 1069–1077.

Wiltschko, D.V., Chapple, W.M., 1977. Flow of weak rocks in Appalachian plateau folds. AAPG Bulletin 61, 653–670.

Zehnder, A.T., Allmendinger, R.W., 2000. Velocity field for the trishear model. Journal of Structural Geology 22, 1009–1014.

Zoetemeijer, R., Sassi, W., Roure, F., Cloetingh, S., 1992. Stratigraphic and kinematic modeling of thrust evolution, northern Apennines, Italy. Geology 20, 1035–1038.